plasma

Article

Influence of Voltage Rising Time on the Characteristics of a Pulsed Discharge in Air in Contact with Water: Experimental and 2D Fluid Simulation Study

Antoine Herrmann, **Joëlle Margot** and **Ahmad Hamdan** *

Groupe de Physique des Plasmas, Département de Physique, Université de Montréal,
Montréal, QC H2V 0B3, Canada; antoine.herrmann@umontreal.ca (A.H.); joelle.margot@umontreal.ca (J.M.)
* Correspondence: ahmad.hamdan@umontreal.ca; Tel.: +1-514-343-2288

Abstract: In the context of plasma–liquid interactions, the phase of discharge ignition is of great importance as it may influence the properties of the produced plasma. Herein, we investigated the influence of voltage rising time (τ_{rise}) on discharge ignition in air as well as on discharge propagation on the surface of water. Experimentally, τ_{rise} was adjusted to 0.1, 0.4, 0.6, and 0.8 kV/ns using a nanosecond high-voltage pulser, and discharges were characterized using voltage/current probes and an ICCD camera. Faster ignition, higher breakdown voltage, and greater discharge current (peak value) were observed at higher τ_{rise}. ICCD images revealed that higher τ_{rise} also promoted the formation of more filaments, with increased radial propagation over the water surface. To further understand these discharges, a previously developed 2D fluid model was used to simulate discharge ignition and propagation under various τ_{rise} conditions. The simulation provided the spatiotemporal evolution of the E-field, electron density, and surface charge density. The trend of the simulated position of the ionization front is similar to that observed experimentally. Furthermore, rapid vertical propagation (<1 ns) of the discharge towards the liquid surface was observed. As τ_{rise} increased, the velocity of discharge propagation towards the liquid increased. Higher τ_{rise} values also led to more charges in the ionization front propagating at the water surface. The discharge ceased to propagate when the charge number in the ionization front reached 0.5×10^8 charges, irrespective of the τ_{rise} value.

Keywords: streamer discharge; numerical simulation; fluid model; discharge in contact with liquid; time-resolved imaging; voltage rising time

check for updates

Citation: Herrmann, A.; Margot, J.; Hamdan, A. Influence of Voltage Rising Time on the Characteristics of a Pulsed Discharge in Air in Contact with Water: Experimental and 2D Fluid Simulation Study. *Plasma* **2024**, 7, 616–630. https://doi.org/10.3390/plasma7030032

Academic Editors: Dariusz Z. Korzec and Maik Froehlich

Received: 25 May 2024
Revised: 11 July 2024
Accepted: 1 August 2024
Published: 5 August 2024

1. Introduction

When an electric field (E-field) is applied to a gaseous dielectric medium, the neutral molecules of the latter can become ionized by the impact of high-energy electrons, leading to the initiation and propagation of a discharge [1]. The separation of charges at the front of the ionization wave produces a high-magnitude space charge field [2,3]. If the magnitude of this field is comparable to that of the breakdown field (35 kV/cm for air at atmospheric pressure), the discharge transits to a streamer [4]. In general, a streamer is characterized by a non-equilibrium thermodynamic plasma channel [5] that propagates with high speed under the action of the space charge field at its head, with the assistance of photoionization to produce seed electrons ahead of its front [6]. Such unique properties promote the application of streamer discharges in various fields such as medicine [7], water depollution [5], and surface treatment [8]. Regardless of the application, better understanding of discharge ignition and plasma–surface interactions is needed to achieve the desired results [9,10].

Since the E-field is a primary factor influencing discharge dynamics, it is essential to understand the influence of voltage amplitude and application period on discharge ignition and propagation in a gap as well as on a surface. At a higher magnitude of the applied voltage, i.e., higher E-field, it is expected that the ionization of gas will occur earlier, and thus, a streamer will be established more quickly [11]. Li et al. [12] numerically demonstrated that by increasing the voltage magnitude from 92 to 112 kV, which corresponded to an increase of a field from 23 to 25 kV/cm, the discharge ignition time decreased from 8.50 to 3.75 ns. The propagation velocity of the discharge in the gap also increased from 0.25 to 0.40 mm/ns. Bourdon et al. [13] simulated discharge propagation in the gap between a pin and plane electrodes, and they observed that an increase in voltage rising time from 80 to 120 kV/ns led to earlier ignition, increased ignition voltage (from 14.5 to 17.4 kV), and faster propagation towards the plane; the times needed to reach the plane at 80 and 120 kV/ns were 5.83 and 2.03 ns, respectively.

In addition to discharge propagation in a gap, voltage characteristics influence propagation over the surface of a dielectric material, either solid or liquid. Konina et al. [14] simulated the propagation of an atmospheric plasma jet (Ar/N_2 = 90/10 with a nitrogen coflow) positioned at 0.8 mm above a ceramic tube, featuring a series of rectangular cross-sectional channels. They showed that by increasing the voltage magnitude from −20 to −25 kV, the surface ionization wave velocity and maximum electron density increased from 0.2 to 0.5 mm/ns and from 4×10^{13} to $1 \times 10^{14} \mathrm{cm}^{-3}$, respectively. Similarly, Höft et al. [15] highlighted that in a pin-to-liquid configuration with a pulsed applied voltage (9 kV of amplitude and 300 µs of pulse width), an increase in the discharge formation time from ~250 to 254 µs resulted in an increase in the generated charge from 2.8 to 5.2 nC. Yang et al. [16] investigated the impact of the voltage applied on an anode needle placed at 0.1 mm above a bismuth silicon oxide (BSO) crystal with a relative dielectric constant of 56. Using a high-voltage pulse with a rising time of 30 ns, they investigated the influence of the voltage plateau value on the discharge. Their results indicated that when the voltage plateau was increased from 4.0 to 5.5 kV, the propagation speed and maximum propagation distance over the surface increased from 0.1 to 0.4 mm/ns and from 5 to 9 mm, respectively.

When a discharge propagates over a dielectric surface, it tends to form filaments due to electron avalanche-triggered radial destabilization of the ionization wave at the discharge front. Therefore, changes in the voltage magnitude can also affect the filamentation process and the observed pattern. According to Yang et al. [16], the number of filaments increased from 6 to 9 as the voltage magnitude was increased from 4.0 to 5.5 kV. In a previous experimental study on discharge propagation over the surface of water [17], we found that with an increasing (breakdown) voltage from 6 to 10 kV, the number of filaments rose from 10 to 15.

In this paper, we aim to further investigate the impact of voltage rising time on the characteristics of a nanosecond discharge ignited in air and propagating over the surface of water, using both experiments and simulation. Experimentally, the rising period of the high voltage pulse was controlled between 0.1 and 0.8 kV/ns by adjusting its plateau value. The discharges were characterized electrically, by measuring voltage–current waveforms, and optically, by acquiring time-integrated and time-resolved ICCD images. As for the simulation, it was performed using a previously developed 2D fluid model, with some modifications. This simulation was used to capture the ignition of the discharge, the propagation in the gap, as well as the propagation on the water surface. The obtained simulation results allowed for the determination of different characteristics such as the spatiotemporal distribution of the E-field, density of charged species, and surface charge.

2. Experimental Conditions

2.1. Electrical Characterization

As shown in Figure 1a, electrical discharges in air in contact with distilled water were ignited using a nanosecond positive pulsed power supply (NSP 120-20-P-500-TG-H; Eagle Harbor Technologies). The plateau duration of the pulse was fixed at 100 ns, while its magnitude was adjusted between 10 and 20 kV to obtain different values of the rising time (τ_{rise} = 0.4, 0.6, and 0.8 kV/ns). An external resistor of R = 250 Ω was added to the circuit to further decrease τ_{rise} to 0.1 kV/ns. A tungsten rod (diameter of 1 mm) with a mechanically polished tip (pin angle of $\sim 30°$) was used as the anode, whereas a stainless steel rod (60 mm diameter) placed at the bottom of a cylindrical Teflon cell (diameter of 67 mm and height of 5.7 mm) was used as the cathode. The cell was filled with 20 mL of distilled water with a dielectric permittivity of $\varepsilon_r = 80$ and an electrical conductivity of $\sigma = 2$ µS/cm, and the distance between the anode pin and water surface was fixed at 600 µm. A vertically mounted ICCD camera (PIMAX-4: 1024 EMB; Princeton Instruments) was used to monitor the behavior of the plasma emission at the solution surface. This camera is equipped with an RB-type intensifier that covers the wavelength range of 200–850 nm with a quantum efficiency between 2 and 15%, depending on the wavelength. The dimension of the captured zone was 10 mm × 10 mm. A delay generator (Quantum Composers Plus 9518 Pulse Generator) was used to adjust the delay between the ICCD camera and the voltage pulse. Figure 1b presents the discharge emission (20 ns integrated ICCD image) at the water surface for τ_{rise} = 0.8 kV/ns, and it highlights the radial propagation of highly organized plasma filaments over the water surface.

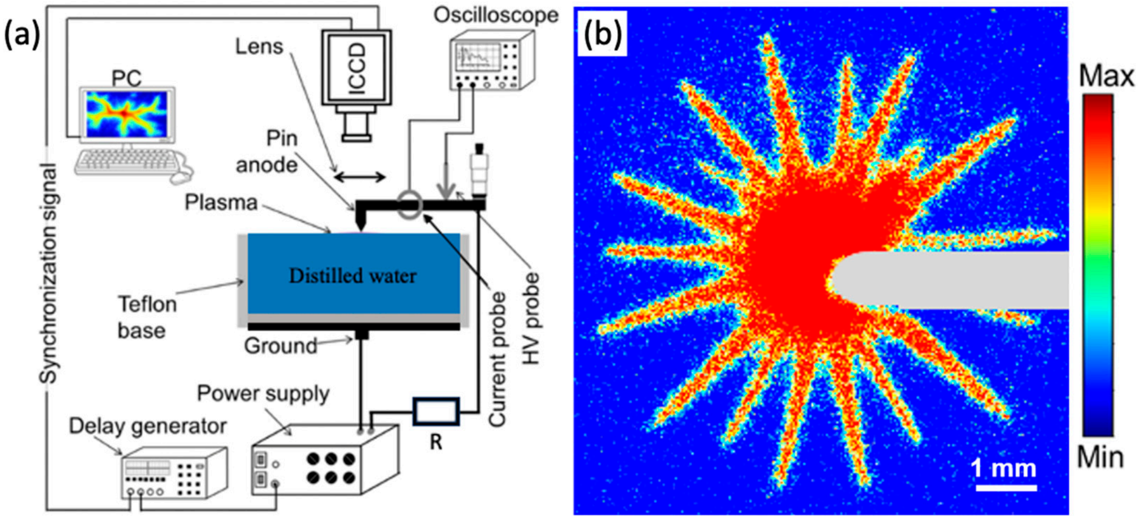

Figure 1. (**a**) Scheme of the experimental setup used to generate nanosecond discharges in air in contact with distilled water. (**b**) 20 ns integrated ICCD camera image of a typical discharge propagating over the water surface for τ_{rise} = 0.8 kV/ns.

The voltage and current characteristics of the discharges were measured using a high-voltage probe (P6015A; Tektronix) and a current monitor (6585; Pearson), respectively. These waveforms were visualized and recorded using an oscilloscope (MSO54, 2 GHz, 6.25 GS/s). Figure 2a,b depict typical voltage–current waveforms of discharges generated under the various conditions of τ_{rise}. Meanwhile, Figure 2c,d provide a closer examination of the region of interest when the discharge occurred at t = 36, 15, 13, and 11 ns for τ_{rise} = 0.1, 0.4, 0.6, and 0.8 kV/ns, respectively. To present the results more clearly, the current waveforms in Figure 2d were all shifted to synchronize with the first peak. For each condition, breakdown occurred during the rising period of the pulse, enabling the investigation of the influence of τ_{rise} on the discharges. For instance, for τ_{rise}= 0.1, 0.4, 0.6, and 0.8 kV/ns, breakdown occurred at a voltage (V_{bd}) of ~4.5, 6.3, 7.8, and 9.1 kV, respectively (Figure 2c). The discharge current (peak value, I_{max}) also depended on τ_{rise}. Indeed, I_{max} increased from 2.2 to 12.9 A as τ_{rise} increased from 0.1 to 0.8 kV/ns. In our experimental setup, the maximal value of the displacement current during the rising time of the applied voltage was around 0.3 A, as highlighted by Hamdan et al. [18] in a previous study. Therefore, it was negligible compared to the current generated by the discharge.

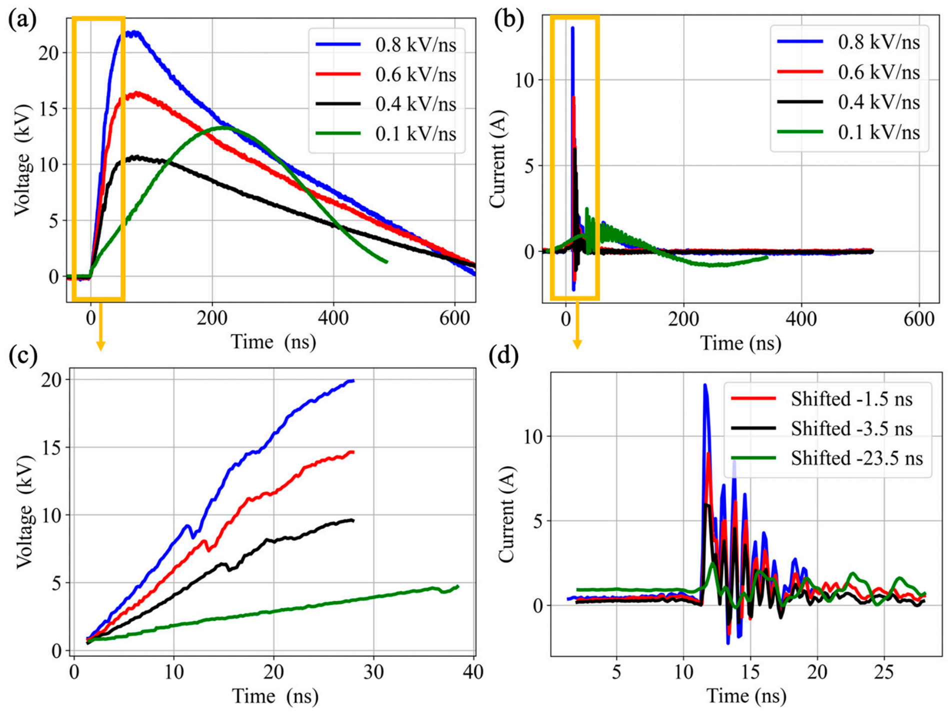

Figure 2. (**a**) Voltage and (**b**) current waveforms of a typical discharge produced with different applied voltages to achieve various rising periods, namely τ_{rise} = 0.1, 0.4, 0.6, and 0.8 kV/ns. (**c**) and (**d**) Zoomed views of the waveforms during the breakdown period.

To account for the stochastic nature of the discharge and accurately capture the typical dispersion of its electrical characteristics, 20 discharges were ignited under each condition. Figure 3a,b illustrate the statistical variation in the formation time (τ_{bd}) and V_{bd} as a function of τ_{rise}. Evidently, τ_{bd} decreased from ~35 ± 2 to 11 ± 1 ns and V_{bd} increased from ~4.5 ± 0.5 to 8.5 ± 2 kV as τ_{rise} was raised from 0.1 to 0.8 kV/ns. This trend will be explained in Section 4.

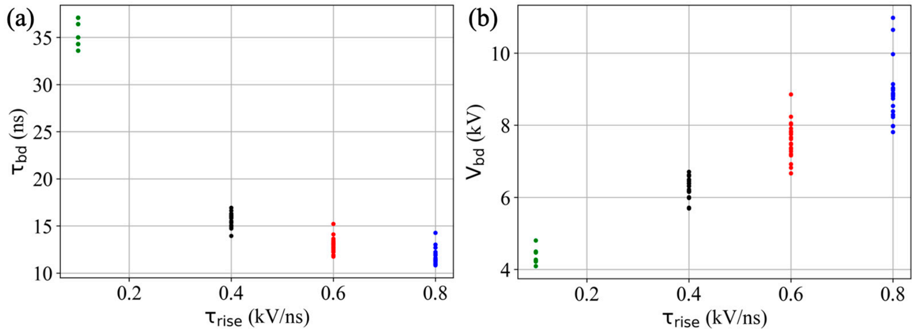

Figure 3. Variation of the (**a**) formation time (τ_{bd}) and (**b**) breakdown voltage (V_{bd}) as a function of the rising time τ_{rise} in the range of 0.1–0.8 kV/ns.

The influence of τ_{rise} on I_{max} is depicted in Figure 4. Notably, the increase in τ_{rise} from 0.1 to 0.8 kV/ns produced an increase in I_{max} from ~2.5 ± 0.7 to 12.5 ± 1.3 A. Therefore, in addition to increased V_{bd}, higher τ_{rise} values led to more intense discharges. This behavior provides insight into the charges generated during breakdown. In fact, Höft et al. [19] also measured that in a pin-to-pin configuration with a 1 mm gap in a gas containing 0.1% O_2 in N_2 at atmospheric pressure, an increase in τ_{rise} (with a plateau value of 10 kV) from 0.0075 to 0.2 kV/ns caused an increase in the maximal current value generated by the discharge from 125 to 175 mA, as well as an increase in the transferred charge from 1.5 to 3.5 nC.

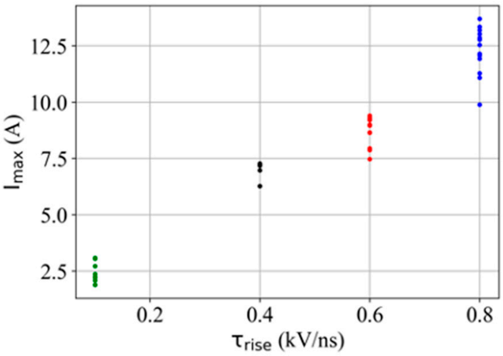

Figure 4. Variation of discharge current (peak value, I_{max}) as a function of the rising time τ_{rise} in the range of 0.1–0.8 kV/ns.

2.2. ICCD Imaging

To elucidate the influence of τ_{rise} on the dynamics of the discharge at the water surface, 20 ns integrated ICCD images of the discharge emission were recorded. Figure 5a shows images of typical discharges occurring at τ_{rise} = 0.1, 0.4, 0.6, and 0.8 kV/ns. Qualitatively, the images show that both the maximal propagation radius (r_{max}) and the number of filaments (plasma dots, i.e., individual surface discharge channels) N_{dots} increased with increasing τ_{rise}. Statistical analysis of numerous acquired ICCD images revealed that when τ_{rise} was increased from 0.1 to 0.8 kV/ns, r_{max} and N_{dots} increased from ~1.7 ± 0.3 to 4.0 ± 0.2 mm (Figure 5b) and from ~10 ± 1 to 20 ± 3 (Figure 5c), respectively. Such increases may be attributed to the increased discharge current at higher τ_{rise}, which signifies a greater number of accumulated charges above the liquid surface. Note that since the ICCD images were integrated during 20 ns and the discharges were ignited only 10–50 ns after applying the voltage pulse, the timescale was too short to observe any Taylor cone formation such as the one described by Yoon et al. [20] as its formation time was on the order of microseconds. Moreover, the 20 consecutive discharges were run at low frequency (1 Hz), which made them not coupled in time and the liquid surface remained steady. The evaporation of the liquid can be neglected as the liquid was replaced after each experiment and the gap distance was adjusted after each set of 20 consecutive discharges.

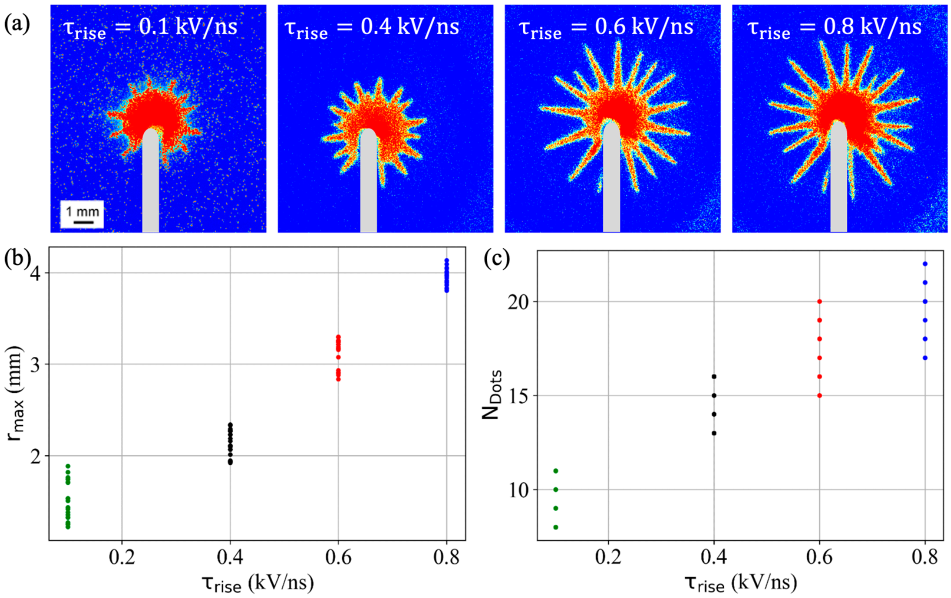

Figure 5. (**a**) 20 ns integrated ICCD images recorded at 0.1, 0.4, 0.6, and 0.8 kV/ns. Variation in (**b**) r_{max} and (**c**) N_{dots} as a function of τ_{rise}.

Figure 6 shows the temporal evolution of the discharge emission over the water surface (1 ns integrated images) during the first 5 ns for all τ_{rise} conditions. In fact, the streamer discharge reached the liquid surface in less than 1 ns (i.e., unresolved here). Then, radial propagation took place over the liquid surface. During the first nanosecond, the emission was disc-like, while 1 ns later, it expanded radially and took the form of a ring-like structure. Then the ring continued to expand radially, and it broke into multiple single plasma dots at t = 3 ns for τ_{rise} = 0.4, 0.6, and 0.8 kV/ns and at t = 4 ns for τ_{rise} = 0.1 kV/ns. Finally, these plasma dots continued to expand radially until they faded away.

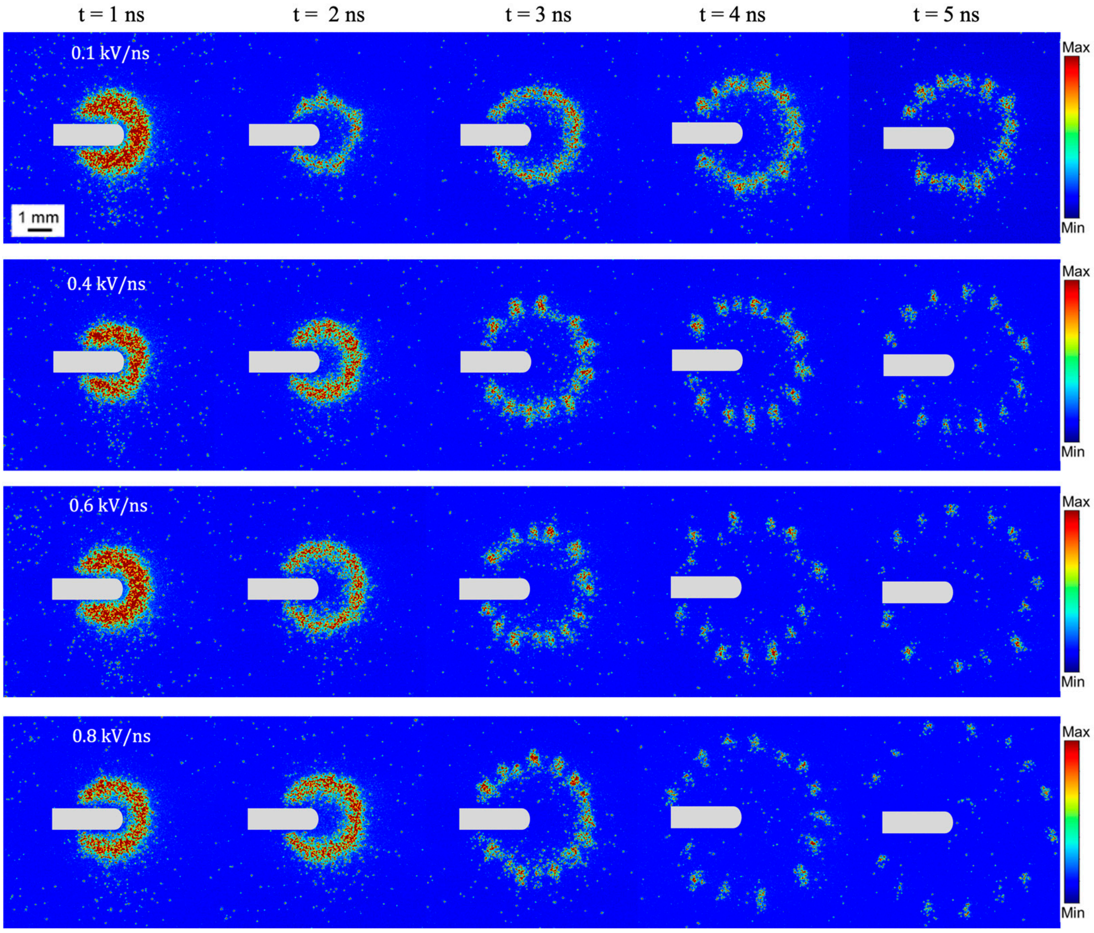

Figure 6. 1 ns integrated ICCD images recorded at 0.1, 0.4, 0.6, and 0.8 kV/ns at t = 1, 2, 3, 4, and 5 ns.

3. Numerical Simulation

3.1. Discharge Model Equations, Boundary Conditions, and Computational Domain

Numerical simulations were conducted by employing a 2D axisymmetric cylindrical fluid model in air at atmospheric pressure. This model solves drift–diffusion equations, yielding the temporal evolution of electron (n_e), positive ion (n_i), and negative ion (n_n) densities. All requisite coefficients, including the diffusion, mobility, gain terms (electron impact ionization, photoionization, and secondary electrons), and loss terms (electron attachment and recombination) were considered electric field-dependent. The liquid was treated as a solid dielectric because its corresponding free charge reorganization time ($\tau_r = \varepsilon_r \varepsilon_0 / \sigma$ = 3540 ns) was much longer than the typical timescale of discharge propagation (between 10 and 40 ns). Additionally, secondary electron emission was considered when positive ions hit the liquid surface. Dielectric surface charging was also incorporated in the model by including fluxes of charged species towards the liquid surface. The electric field distribution in the computational domain was determined by resolving Poisson's equation.

Meanwhile, photoionization was addressed by solving Helmholtz's equations, according to the Finite Volume Method wherein charged species fluxes were computed based on the Scharfetter–Gummel scheme. Poisson's and Helmholtz's equations were solved using a direct solver in Python, and the Ghost Fluid Method was used to enhance the geometric accuracy in simulating the pin boundary. The 2nd order Runge–Kutta method was adopted for the integration of the fluid equations, and the time step was determined based on Courant–Friedrichs–Lewy (CFL) conditions. Moreover, an electron flux correction was implemented to circumvent the restriction of the dielectric relaxation time and optimize the computational efficiency. A comprehensive description of all transport coefficients and numerical methods employed herein can be found in [21].

Boundary conditions for n_e, n_i, n_n, and Helmholtz's equations were the same as those described in [21]. Likewise, for Poisson's equation, we employed the same boundary conditions as in [21], except for the Dirichlet boundary condition value at the anode. Herein, a dielectric (with a thickness of 500 µm and $\varepsilon_r = 2$) was added between the ground and the water to reproduce the experimental setup.

The background density of electrons and ions ($n_{e,i}$) was fixed at $10^9 \mathrm{m}^{-3}$, and the initial density of n_n was set to 0. To optimize the computational time, a non-uniform grid was used, with high resolution near the regions of interest such as the liquid surface. As shown in Figure 7, the simulation was performed on a $10.4 \times 6\ \mathrm{mm}^2$ rectangular domain with a grid size of 1082×1001. Along the axial direction z, the dimensions used were the following:

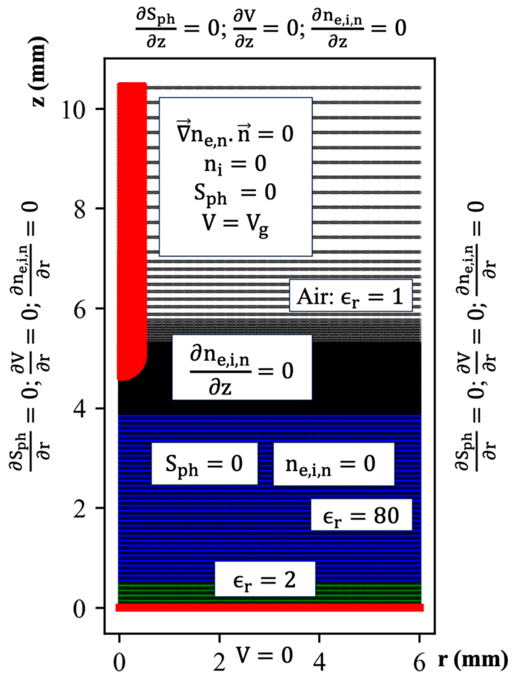

Figure 7. Simulation domain showing the parameters and boundary conditions. The grid is shown in the background.

- From $z = 0$ to 3.9 mm, uniform grid with $\Delta z = 20$ µm;
- From $z = 3.9$ to 4.2 mm, uniform grid with $\Delta z = 0.7$ µm;
- From $z = 4.2$ to 4.5 mm, non-uniform grid with a geometric expansion $\Delta z_i = 1.1 \Delta z_{i-1}$ up to $\Delta z = 3.65$ µm;
- From $z = 4.5$ to 5.1 mm, uniform grid with $\Delta z = 3.65$ µm;
- From $z = 5.1$ to 5.7 mm, non-uniform grid with a geometric expansion $\Delta z_i = 1.1 \Delta z_{i-1}$ up to $\Delta z = 30$ µm;
- From $z = 5.7$ to 10.4 mm, non-uniform grid with a geometric expansion $\Delta z_i = 1.1 \Delta z_{i-1}$ up to $\Delta z = 60$ µm.

In the radial direction, a uniform grid with $\Delta r = 6$ µm was used between $r = 0$ and 6 mm .

To replicate the experimental pulse, we assumed that the circuit depicted in Figure 8a was representative of the setup. The application of Kirchhoff's voltage law on the circuit yielded the following equation:

$$V_a = RI + V_g \tag{1}$$

where V_a is the voltage applied by the pulser (depicted in Figure 8b), R = 1 kΩ is the pulser resistance [22], I is the total current, and V_g is the voltage across the gap where the discharge occurs.

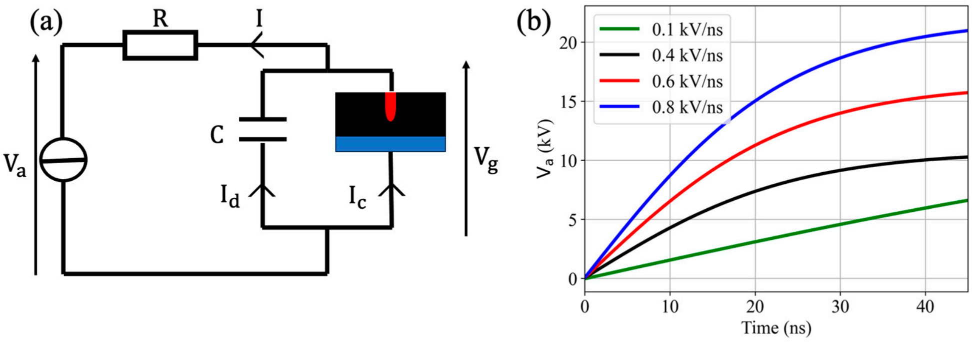

Figure 8. (**a**) Equivalent circuit used for the simulation and (**b**) V_a used to reproduce τ_{rise} = 0.1, 0.4, 0.6, and 0.8 kV/ns.

The circuit capacitance of C = 0.1 pF was estimated experimentally from the voltage–current measurements, based on the following formula, $C = I_d / \frac{\partial V_g}{\partial t}$, where I_d is the displacement current. A more comprehensive equivalent circuit could be constructed, similar to the one developed in a previous study by Mericiris et al. [22]. However, for simplicity, computational efficiency, and due to the good agreement between the experimental and simulation results presented hereafter, we believe that this representation is satisfactory. Considering that $I = I_d + I_c$, where I_c is the conduction current resulting from the discharge (calculated based on the extended Sato method [11]), Equation (1) was rearranged as

$$RC\frac{\partial V_g}{\partial t} + V_g = V_a - RI_c \tag{2}$$

Knowing the values of R, C, V_a, and I_c, V_g was determined by resolving Equation (2). To assess the effect of τ_{rise} on discharge dynamics, four simulations were conducted at $\tau_{rise} = 0.1$, 0.4, 0.6, and 0.8 kV/ns. The value of τ_{rise} was varied by adjusting the waveform of V_a, as shown in Figure 8b.

3.2. Simulation Results

3.2.1. Electrical Results

Figure 9a,b display the temporal evolution of the simulated V_g and I_c values. Despite variations in the breakdown voltage and breakdown moment, the simulated voltage waveform is in excellent agreement with the experimental one (Figure 2c). Specifically, the simulated results show that the increase of τ_{rise} from 0.1 to 0.8 kV/ns led to earlier breakdown (delay decreases from ~30 to 7 ns) and higher breakdown voltage (increases from ~3.7 to 5.9 kV)—a trend similar to the one observed experimentally. Moreover, the numerical model accurately captured the voltage drop caused by the intense current generation due to the ignition of the discharge, as observed experimentally in Figure 2c. Figure 8b shows the simulated discharge current, which is also similar to the experimental one. Indeed, I_{max} increased from ~0.6 to 1.9 A as τ_{rise} was raised from 0.1 to 0.8 kV/ns. Note that for all investigated conditions, the simulated I_{max} values are lower than the experimental ones, probably due to the lower breakdown voltage obtained numerically (approximately 1.5 times lower) compared to the experimental breakdown. The absence of oscillations from the simulated waveform was due to the fact that the voltage probe characteristics and RLC parasitic circuit were not considered in the simulation. Overall, the electrical characteristics simulated using the simplified circuit are comparable to those obtained experimentally, which indicates that the model is valid and can be used to analyze other plasma properties.

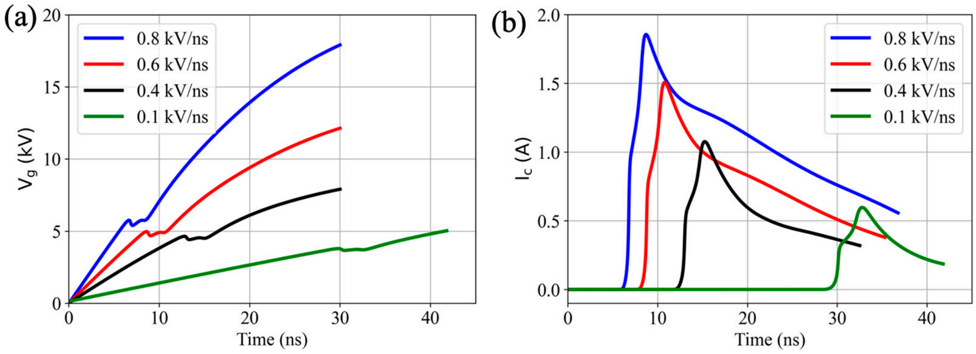

Figure 9. Temporal evolution of simulated (**a**) V_g and (**b**) I_c at τ_{rise} conditions of 0.1, 0.4, 0.6, and 0.8 kV/ns.

3.2.2. Vertical Propagation

Considering that ignition occurs at different times (t_{ign}) for different discharge events, the following results are presented with t_{ign} as a reference. Following ignition, an ionization wave (IW) propagated in the gap and reached the water surface in less than 1 ns. Since the vertical propagation of the discharge towards the liquid surface occurred in less than 1 ns, and given the stochastic nature of discharge ignition, even with an integration time as short as 1 ns, we were unable to accurately capture the vertical propagation of the discharge experimentally. Therefore, we decided to investigate it through simulation. Figure 10 depicts the temporal evolution of the E-field under various conditions of τ_{rise}. The propagation of the IW was mainly driven by the space charge field, and it was clearly affected by τ_{rise}, as the produced E-field was strongly dependent on this parameter. Indeed, for a comparable time and/or comparable position, the field was higher for higher τ_{rise}. As the IW propagated in the gap, the E-field magnitude increased and reached a peak value when the IW touched the liquid surface; this was due to the accumulation of charges on the liquid surface. For instance, at τ_{rise} = 0.8 kV/ns, the IW reached the water surface at 0.8 ns after breakdown, and the peak value of the electric field was ~700 kV/cm.

Figure 11a displays the position of the IW as a function of time for different τ_{rise} conditions (solid lines). The magnitude of the axial propagation velocity ($\left\|\vec{v}_z\right\|$) of the IW is also shown in Figure 11a (dotted lines). Clearly, τ_{rise} had a significant effect on the propagation of the IW in the gap. At τ_{rise} = 0.1 kV/ns, the IW reached the liquid surface 1.5 ns after ignition, while at τ_{rise} = 0.8 kV/ns, it reached the surface 0.80 ns after ignition. As the IW traveled towards the liquid, $\left\|\vec{v}_z\right\|$ increased, reaching maximum just before approaching the liquid surface. Obviously, $\left\|\vec{v}_z\right\|$ tended to zero when it touched the liquid surface. The higher the τ_{rise}, the higher the $\left\|\vec{v}_z\right\|_{max}$. For instance, $\left\|\vec{v}_z\right\|_{max}$ increased from 0.75 to 1.25 mm/ns when τ_{rise} increased from 0.1 to 0.8 kV/ns. Figure 11b shows the evolution of E_{max} (at the IW head) as a function of time for different τ_{rise} conditions. The results also show that E_{max} was higher at higher τ_{rise} values, not only during propagation in the air gap but also when reaching the water surface.

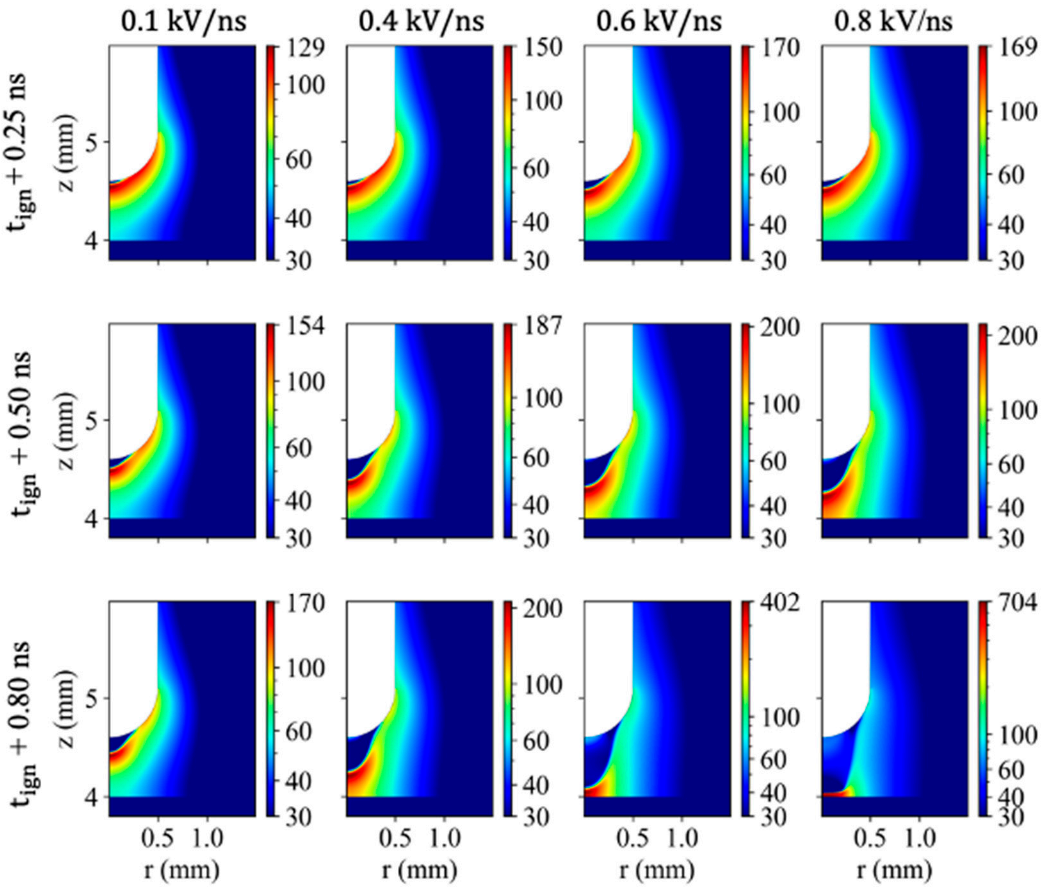

Figure 10. Spatiotemporal evolution of the E-field (kV/cm) during the propagation of the discharge in the gap towards the liquid surface for τ_{rise} = 0.1, 0.4, 0.6, and 0.8 kV/ns.

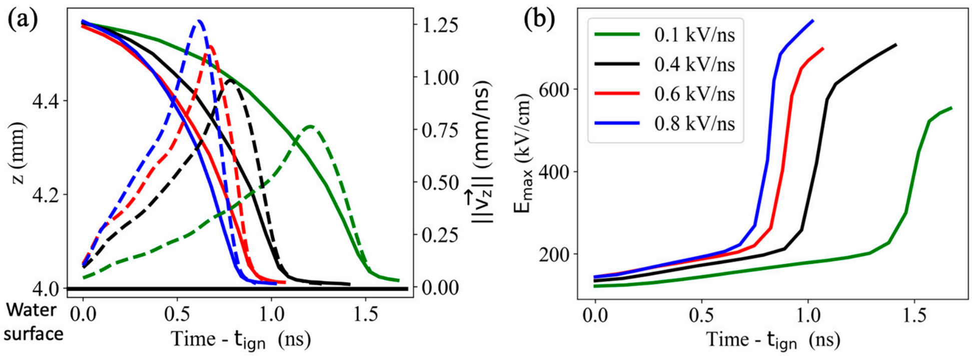

Figure 11. Temporal evolution of (**a**) the position (solid lines) and the propagation velocity ($\left\|\vec{v_z}\right\|$) of the IW (dotted lines). (**b**) Maximal E-field generated by the IW for τ_{rise} = 0.1, 0.4, 0.6, and 0.8 kV/ns.

3.2.3. Radial Propagation

When the IW reaches a water surface, charges accumulate and produce a radial electric field that may ignite a surface discharge [23]. Herein, the propagation of the surface IW (SIW) was investigated under different conditions of τ_{rise}. Figure 12a,b show the spatiotemporal evolution of the E-field and n_e for the different τ_{rise} values; t_s is defined as the moment when the IW reaches the liquid surface. At t_s + 1 ns, the SIW propagated relatively longer and the E_{max} was relatively higher at higher τ_{rise}. For instance, the values of r and E_{max} determined at τ_{rise} = 0.1 kV/ns were 0.4 mm and 650 kV/cm, compared to 0.75 mm and 1200 kV/cm at τ_{rise} = 0.8 kV/ns, respectively. Unlike r and E_{max}, $n_{e_{max}}$ remained almost constant (~5–7 $\times$ 10^{20} m^{-3}), irrespective of the τ_{rise} condition. As the SIW propagated on the liquid surface, the radial position of the SIW changed significantly; for instance, at t_s + 8 ns, we noted that r = 0.85 mm for τ_{rise} = 0.1 kV/ns and r = 1.9 mm for τ_{rise} = 0.8 kV/ns. However, the E_{max} and $n_{e_{max}}$ values remained within the same order for all conditions, with E_{max} ~860 kV/cm and $n_{e_{max}}$ ~5 × 10^{20} m^{-3}. In our study, no back discharge on the pin surface was observed, contrary to what Höft et al. [15] observed in some cases. This difference can be attributed to our pin not being covered by a dielectric, thereby limiting surface propagation by preventing surface charging.

(a) E-field distribution

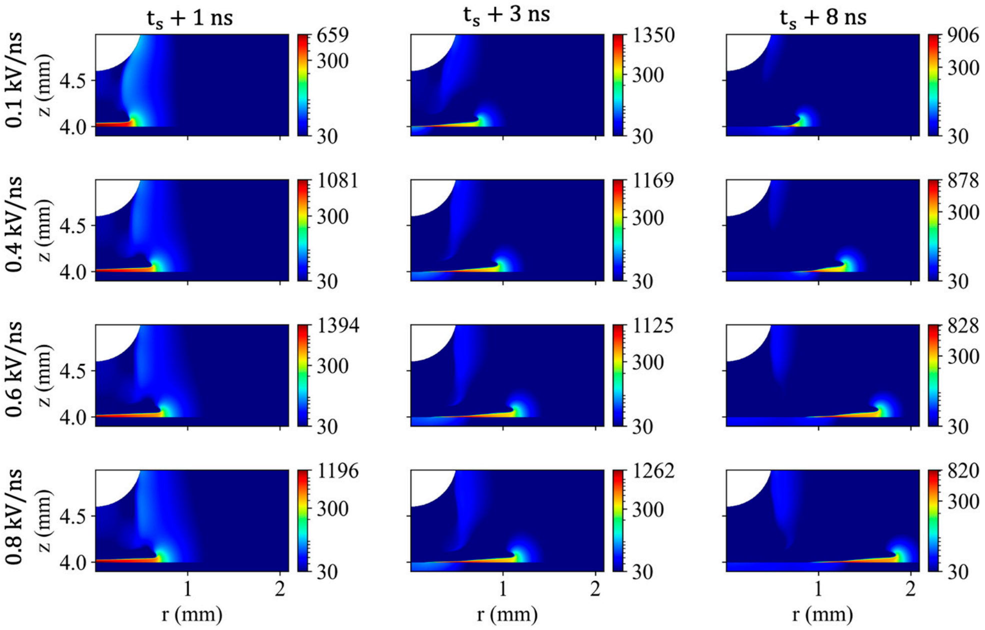

(b) n_e distribution

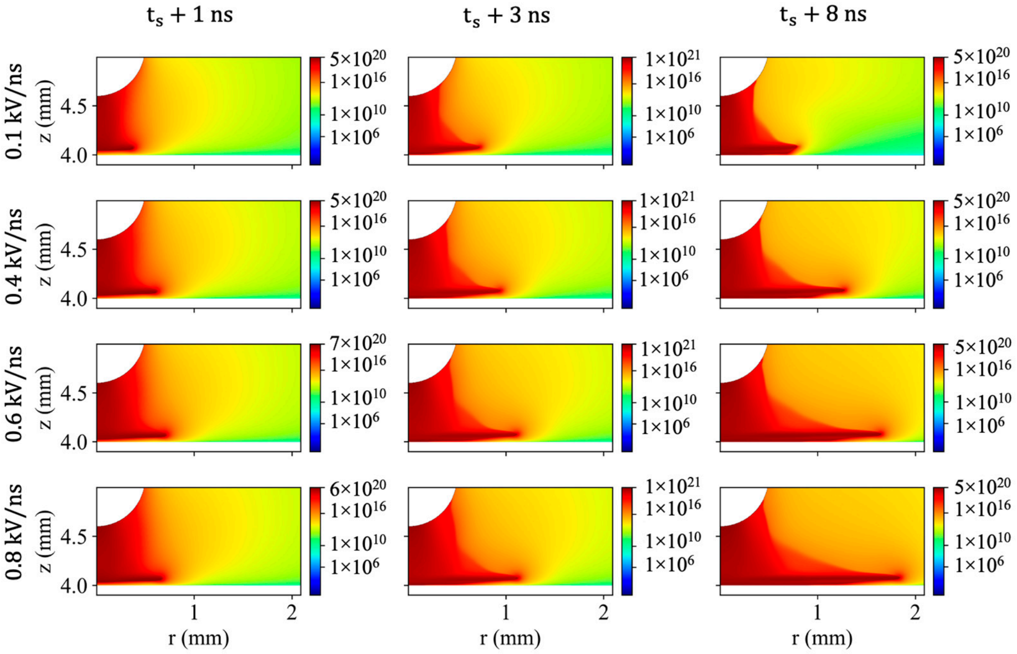

Figure 12. Spatiotemporal evolution of the (**a**) E-field (kV/cm) and (**b**) electron density (m^{-3}) distributions during SIW propagation for τ_{rise} = 0.1, 0.4, 0.6, and 0.8 kV/ns.

Figure 13 compares the simulation-derived and experimentally determined temporal evolution of the SIW position over the liquid surface. The experimental data were obtained by processing numerous 1 ns integrated ICCD images recorded at different times during SIW propagation (as illustrated on Figure 6) using a custom algorithm [17]. The simulated positions of the SIW were determined by identifying the maximal value of the ionization term at each moment, following the methodology outlined in [21]. As shown in Figure 13, the simulated temporal evolution profiles of the SIW position are in good agreement with the experimental profiles, irrespective of the τ_{rise} condition. However, the simulated r_{max} values are slightly lower than those determined experimentally. This difference is likely due to the numerical breakdown occurring at relatively lower V_{bd}, which resulted in a lower background field in the air gap, thereby limiting the radial propagation in the simulations compared to the experimental results. Overall, the data indicate that both the propagation velocity and maximal radial position of the SIW increased at higher τ_{rise}.

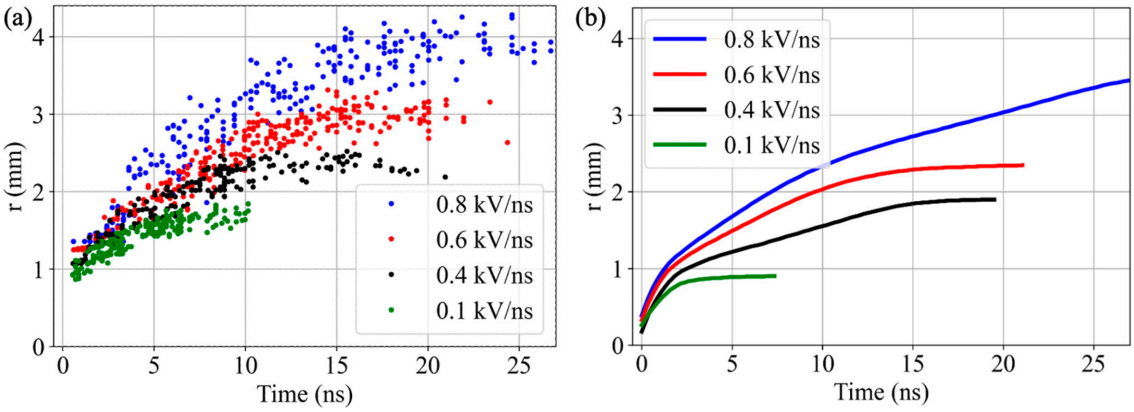

Figure 13. Temporal evolution of the radial position of the discharge over the liquid surface for τ_{rise} = 0.1, 0.4, 0.6, and 0.8 kV/ns: (**a**) experimental data and (**b**) data derived from the simulation.

4. Discussion

4.1. Impact of τ_{rise} on Discharge Ignition

It was feasible to estimate the ignition time of a streamer discharge under a given E-field using analytical formulas derived from the 1st Townsend coefficient. This coefficient offers an estimation of when a sufficient number of charged species are generated to initiate a streamer discharge [24]. However, in our case, breakdown occurred during the voltage rising period. As a result, the E-field was time-dependent and we could not estimate the formation time for a given E-field. Figure 14a illustrates the temporal evolution of the maximum E-field in the gap (from simulation) under various conditions of τ_{rise}. The yellow dotted line represents the breakdown field in air (E_{bd}~35 kV/cm). Increasing τ_{rise} made reaching the breakdown field faster; for instance, E_{max} exceeded 35 kV/cm at t = 1.4 ns for τ_{rise} = 0.8 kV/ns, while it was reached at t = 6.2 ns for τ_{rise} = 0.1 kV/ns. The change in slopes for E_{max} across all conditions was attributed to discharge ignition, where the space charge field generated by the discharge surpassed the maximum Laplacian field measured before ignition (identified by the arrow for each condition on Figure 14a). Figure 14b depicts the temporal variation in the number of charged species (N_s) generated at the anode tip. $N_s = 10^8$ represents Meek's criterion, indicating the number of charged species needed to initiate a streamer discharge (marked by a yellow dotted line in the figure). Clearly, this criterion was met more rapidly at higher τ_{rise}, which suggests that charged species were more easily produced at this condition. Indeed, Meek's criterion was satisfied at t = 5.2 and 28 ns for τ_{rise} = 0.8 and 0.1 kV/ns, respectively.

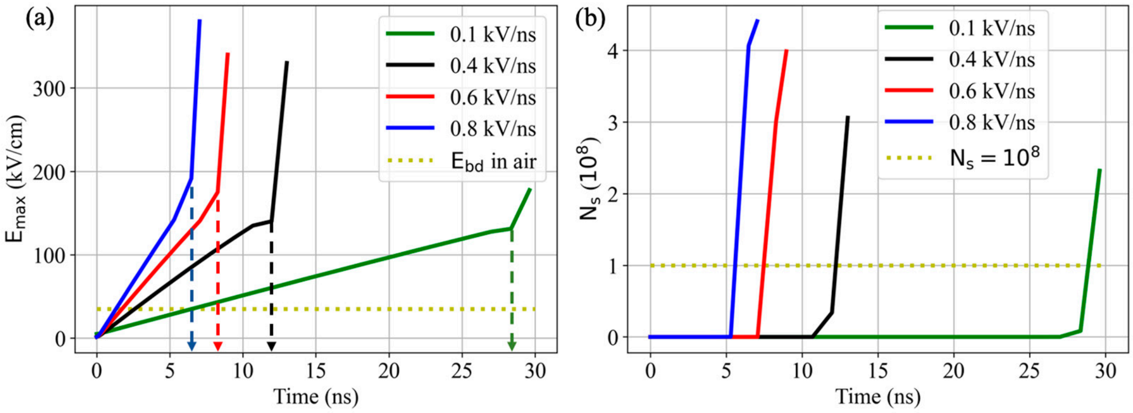

Figure 14. Temporal evolution of (**a**) the maximal electric field generated (E_{max}) and of (**b**) the number of charged species created near the tip of the anode for $\tau_{rise} = 0.1,\ 0.4,\ 0.6,$ and 0.8 kV/ns.

4.2. Impact of τ_{rise} on the E-Field and N_s during the Radial Propagation

The observed trend of SIW radial propagation can be understood by examining the radial electric field. Figure 15a shows that initially, i.e., once the SIW was ignited, the maximum radial field (Er_{max}) increased with increasing τ_{rise}. Indeed, within the investigated τ_{rise} range of 0.1–0.8 kV/ns, the peak value of Er_{max} increased from ~245 to 346 kV/cm. This increase is attributed to a greater accumulation of charges induced by the increased initial electric field, as V_{bd} was higher at high τ_{rise}. As the SIW propagated radially, Er_{max} decreased after ignition for all conditions. However, at a given time, Er_{max} remained higher for higher τ_{rise} values. For instance, at t = 6 ns, Er_{max} increased from 146 to 279 kV/cm when τ_{rise} was raised from 0.1 to 0.8 kV/ns. The increase in the electric field further promoted the production of charged species, thereby contributing to the experimentally observed increase in I_{max}, as highlighted in Figure 4.

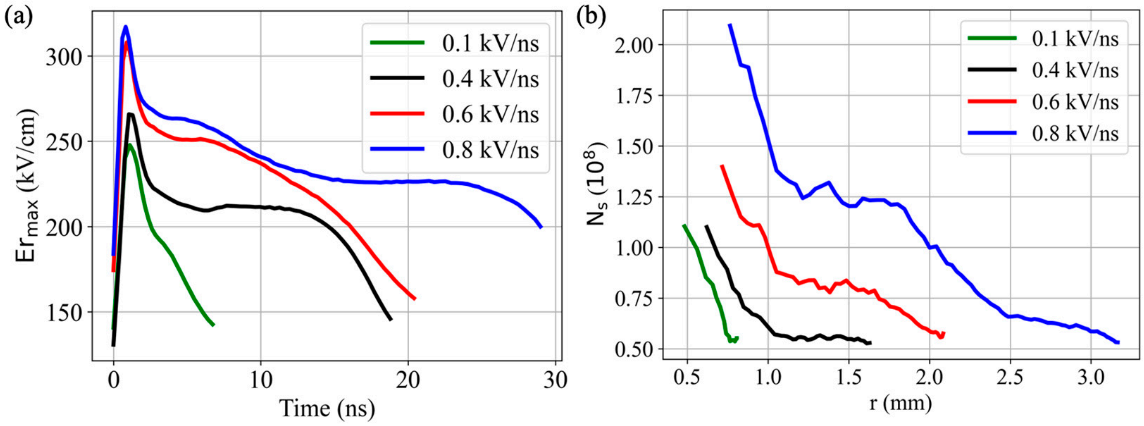

Figure 15. (**a**) Temporal evolution of the maximal radial electric field (Er_{max}) generated by the SIW and (**b**) radial profile of the number of charged species (N_s) created by the streamer's head for $\tau_{rise} = 0.1,\ 0.4,\ 0.6,$ and 0.8 kV/ns.

Finally, Figure 15b shows the variation in N_s during the radial propagation of the SIW over the liquid surface for all τ_{rise} conditions. The method used to determine N_s was based on both the simulation and experimental results, and it is detailed elsewhere [21]. At a given radial position, we observed that N_s increased with increasing τ_{rise}. For example, when τ_{rise} was increased from 0.1 to 0.8 kV/ns at r = 0.75 mm, N_s rose from 0.5×10^8 to 2.1×10^8. The relatively high values of N_s, i.e., verifying Meek's criterion, indicated that the SIW may have been identified as a surface streamer discharge. For all the conditions, N_s

decreased as the SIW propagated radially, and notably, SIW ceased propagation at almost the same N_s value of $\sim 0.5 \times 10^8$.

5. Conclusions

In this study, experimental and numerical approaches were used to investigate the influence of voltage rising time (τ_{rise}) on discharges generated in air using a pin-to-water setup. Experimentally, it was observed that the discharge ignition time was reduced from 35 to 12 ns upon increasing τ_{rise} in the range of 0.1–0.8 kV/ns. Meanwhile, the breakdown voltage and maximal discharge current were increased from 4.5 to 8 kV and from 2.2 to 12.9 A, respectively. The simulation results showed similar trends, albeit with smaller values. These trends may be attributed to the rapid generation of an intense E-field at higher τ_{rise}, which facilitated the attainment of Meek's criterion (i.e., high number of charges) near the pin tip.

The simulation also captured the propagation of the discharge in the gap towards the liquid surface and showed that the maximal propagation velocity increased (from 0.75 to 1.25 mm/ns) at higher τ_{rise} (0.1–0.8 kV/ns), while the time needed for the ionization wave (IW) to reach the liquid surface decreased (from 1.5 to 0.8 ns).

Analysis of the propagation of the surface ionization wave (SIW) on the water surface revealed that when τ_{rise} was increased (from 0.1 to 0.8 kV/ns), a number of filaments formed over the surface and their maximal radial propagation increased (from 10 to 25 and from 1.7 to 4.1 mm, respectively). Such an increase may be attributed to the higher initial E-field generated by the filament at a higher τ_{rise}.

Based on the experimental and simulation findings, we determined that more charges accumulated in the discharge head upon increasing τ_{rise}. For all τ_{rise} conditions, SIW propagation was arrested when the number of charges reached 0.5×10^8.

Author Contributions: Conceptualization, A.H. (Antoine Herrmann) and A.H. (Ahmad Hamdan); methodology, A.H. (Antoine Herrmann) and A.H. (Ahmad Hamdan); validation, A.H. (Antoine Herrmann) and A.H. (Ahmad Hamdan); formal analysis, A.H. (Antoine Herrmann) and A.H. (Ahmad Hamdan); data curation, A.H. (Antoine Herrmann); writing—original draft preparation, A.H. (Antoine Herrmann); writing—review and editing, A.H. (Ahmad Hamdan) and J.M.; supervision, A.H. (Ahmad Hamdan); project administration, A.H. (Ahmad Hamdan); funding acquisition, A.H. (Ahmad Hamdan). All authors have read and agreed to the published version of the manuscript.

Funding: This research was funded by the Natural Sciences and Engineering Research Council of Canada (NSERC), grant number RGPIN-2023-03951, and The APC was waived by the Journal.

Data Availability Statement: The data that support the findings of this study are available within this article.

Conflicts of Interest: The authors declare no conflicts of interest.

References

1. Kulikovsky, A.A. Analytical model of positive streamer in weak field in air: Application to plasma chemical calculations. *IEEE Trans. Plasma Sci.* **1998**, *26*, 1339–1346. [CrossRef]
2. Li, C.; Teunissen, J.; Nool, M.; Hundsdorfer, W.; Ebert, U. A comparison of 3D particle, fluid and hybrid simulations for negative streamers. *Plasma Sources Sci. Technol.* **2012**, *21*, 055019. [CrossRef]
3. Teunissen, J. Improvements for drift-diffusion plasma fluid models with explicit time integration. *Plasma Sources Sci. Technol.* **2020**, *29*, 015010. [CrossRef]
4. Montijn, C.; Ebert, U. Diffusion correction to the Raether-Meek criterion for the avalanche-to-streamer transition. *J. Phys. D Appl. Phys.* **2006**, *39*, 2979–2992. [CrossRef]
5. Rezaei, F.; Vanraes, P.; Nikiforov, A.; Morent, R.; De Geyter, N. Applications of plasma-liquid systems: A review. *Materials* **2019**, *12*, 2751. [CrossRef]
6. Bagheri, B.; Teunissen, J.; Ebert, U.; Becker, M.M.; Chen, S.; Ducasse, O.; Eichwald, O.; Loffhagen, D.; Luque, A.; Mihailova, D.; et al. Comparison of six simulation codes for positive streamers in air. *Plasma Sources Sci. Technol.* **2018**, *27*, 095002. [CrossRef]
7. Laroussi, M. Plasma Medicine: A Brief Introduction. *Plasma* **2018**, *1*, 47–60. [CrossRef]
8. Kim, M.C.; Yang, S.H.; Boo, J.-H.; Han, J.G. Surface treatment of metals using an atmospheric pressure plasma jet and their surface characteristics. *Surf. Coat. Technol.* **2003**, *174*, 839–844. [CrossRef]

9. Celestin, S.; Allegraud, K.; Canes-Boussard, G.; Leick, N.; Guaitella, O.; Rousseau, A. Patterns of plasma filaments propagating on a dielectric surface. *IEEE Trans. Plasma Sci.* **2008**, *36*, 1326–1327. [CrossRef]
10. Meyer, H.K.H.; Marskar, R.; Mauseth, F. Evolution of positive streamers in air over non-planar dielectrics: Experiments and simulations. *Plasma Sources Sci. Technol.* **2022**, *31*, 114006. [CrossRef]
11. Eichwald, O.; Ducasse, O.; Dubois, D.; Abahazem, A.; Merbahi, N.; Benhenni, M.; Yousfi, M. Experimental analysis and modelling of positive streamer in air: Towards an estimation of O and N radical production. *J. Phys. D Appl. Phys.* **2008**, *41*, 23. [CrossRef]
12. Li, X.; Sun, A.; Zhang, G.; Teunissen, J. A computational study of positive streamers interacting with dielectrics. *Plasma Sources Sci. Technol.* **2020**, *29*, 065004. [CrossRef]
13. Bourdon, A.; Péchereau, F.; Tholin, F.; Bonaventura, Z.; Study, Z.B. Study of the electric field in a diffuse nanosecond positive ionization wave generated in a pin-to-plane geometry in atmospheric pressure air. *J. Phys. D Appl. Phys.* **2021**, *54*, 075204. [CrossRef]
14. Konina, K.; Raskar, S.; Adamovich, I.V.; Kushner, M.J. Atmospheric pressure plasmas interacting with wet and dry microchannels: Reverse surface ionization waves. *Plasma Sources Sci Technol.* **2024**, *33*, 015002. [CrossRef]
15. Höft, H.; Kettlitz, M.; Brandenburg, R. The role of a dielectric barrier in single-filament discharge over a water surface. *J. Appl. Phys.* **2021**, *129*, 043301. [CrossRef]
16. Yang, X.; Wang, W.; Wang, X.; Du, Y.; Meng, Y.; Wu, K. Experimental study of transient surface charging during dielectric barrier discharges in air gap in needle-to-plane geometry. *J. Phys. D Appl. Phys.* **2023**, *56*, 465202. [CrossRef]
17. Herrmann, A.; Margot, J.; Hamdan, A. Influence of voltage and gap distance on the dynamics of the ionization front, plasma dots, produced by nanosecond pulsed discharges at water surface. *Plasma Sources Sci. Technol.* **2022**, *31*, 045006. [CrossRef]
18. Hamdan, A.; Diamond, J.; Stafford, L. Time-resolved imaging of pulsed positive nanosecond discharge on water surface: Plasma dots guided by water surface. *Plasma Sources Sci. Technol.* **2020**, *29*, 115017. [CrossRef]
19. Höft, H.; Becker, M.M.; Loffhagen, D.; Kettlitz, M. On the influence of high voltage slope steepness on breakdown and development of pulsed dielectric barrier discharges. *Plasma Sources Sci. Technol.* **2016**, *25*, 064002. [CrossRef]
20. Yoon, S.Y.; Jeon, H.; Yi, C.; Park, S.; Ryu, S.; Kim, S.B. Mutual interaction between plasma characteristics and liquid properties in AC-driven pin-to-liquid discharge. *Sci. Rep.* **2018**, *8*, 12037. [CrossRef]
21. Herrmann, A.; Margot, J.; Hamdan, A. Experimental and 2D fluid simulation of a streamer discharge in air over a water surface. *Plasma Sources Sci. Technol.* **2024**, *33*, 025022. [CrossRef]
22. Merciris, T.; Valensi, F.; Hamdan, A. Determination of the Electrical Circuit Equivalent to a Pulsed Discharge in Water: Assessment of the Temporal Evolution of Electron Density and Temperature. *IEEE Trans. Plasma Sci.* **2020**, *48*, 3193–3202. [CrossRef]
23. Zhang, Q.Z.; Zhang, L.; Yang, D.Z.; Schulze, J.; Wang, Y.N.; Bogaerts, A. Positive and negative streamer propagation in volume dielectric barrier discharges with planar and porous electrodes. *Plasma Process. Polym.* **2021**, *18*, e2000234. [CrossRef]
24. Nijdam, S.; Teunissen, J.; Ebert, U. The physics of streamer discharge phenomena. *Plasma Sources Sci. Technol.* **2020**, *29*, 103001. [CrossRef]